

Contents lists available at ScienceDirect

Journal of Chromatography A

journal homepage: www.elsevier.com/locate/chroma



Modelling of analyte profiles and band broadening generated by interface loops used in multi-dimensional liquid chromatography



Ali Moussa^a, Thomas Lauer^b, Dwight Stoll^b, Gert Desmet^a, Ken Broeckhoven^{a,*}

- ^a Vrije Universiteit Brussel, Pleinlaan 2, 1050 Brussel, Belgium
- ^b Gustavus Adolphus College, 800 West College Avenue, Saint Peter, MN, 56082, USA

ARTICLE INFO

Article history: Received 15 July 2021 Revised 17 September 2021 Accepted 21 September 2021 Available online 24 September 2021

Keywords:
Loop dispersion
Numerical simulations
Loop coiling
Peak variance model
Modulation
Two-dimensional liquid chromatography

ABSTRACT

Currently, the shape and variance of the analyte band entering the second dimension column when injected from an open loop interface in two-dimensional liquid chromatography is not fully understood. This is however important as it is connected to several other variables encountered when developing 2D-LC methods, including the first dimension flow rate, the sampling (modulation) time and the loop volume. Both numerical simulation methods and experimental measurements were used to understand and quantify the dispersion occurring in open tubular interface loops. Variables included are the analyte diffusion coefficient (D_{mol}) , loop filling and emptying rates $(F_{fill} \& F_{empty})$, loop inner diameter or radius (R_{loop}) and loop volume (V_{loop}) . For a straight loop capillary, we find that the concentration profile (as measured at the loop outlet) depends only on a single dimensionless parameter $t^*_{empty} = \frac{V_{loop}}{F_{empty}} \cdot \frac{D_{mol}}{R_{loop}^2}$ and the ratio of the filling and emptying flow rates F_{empty}/F_{fill} . A model depending only on these two parameters was developed to predict of the peak variance resulting from the filling and emptying of a straight capillary operated in the first-in-last-out (FILO) modulation mode. Comparison of the concentration profiles and the corresponding variances obtained by either numerical simulation or experiments with straight capillaries shows the results generally agree very well. When the straight capillary is replaced by a tightly coiled loop, significantly smaller (20-40%) peak variances are observed compared to straight capillaries. The magnitude of these decreases is not predicted as well by simulations, however the simulation results are still useful in this case, because they represent an upper boundary (i.e., worst-case scenario) on the predicted variance.

© 2021 Elsevier B.V. All rights reserved.

1. Introduction

The use of analytical scale two-dimensional liquid chromatography (2D-LC) has increased significantly in recent years to address problems that cannot be resolved by conventional one-dimensional LC (1D-LC). It has not only been applied in the so-called "omics"-fields and biopharmaceutical analysis, but also for small molecule analysis in the pharmaceutical and chemical industry [1-4]. One of the main reasons for this evolution is the large increase in commercially available instrumentation and software for 2D-LC. However, method development still remains a bottleneck, in part due to insufficient fundamental understanding of some key aspects of the instrumentation. The major challenges typically encountered during method development include finding the optimal combination of separation mechanisms in each dimension, and overcoming problems associated with the mismatch between the properties of

E-mail address: Ken.Broeckhoven@vub.be (K. Broeckhoven).

the mobile phases used in the two dimensions (e.g., peak splitting due to large injections of "strong solvent" into the second dimension) [1,5].

The process by which fractions of first dimension (¹D) effluent are transferred to the second dimension (2D) column is commonly referred to as "modulation" or "sampling" [6]. The number and volume of fractions collected can also be important determinants of the quality of a 2D-LC separation. For all modes of 2D-LC separation in use today (i.e., from simple single heart-cut (LC-LC) to fully comprehensive (LC \times LC)) [5], it is most common to transfer ¹D effluent to the ²D column using a simple open tubular capillary. These conventional fraction collection loops are in some cases replaced by trap columns, but these applications are outside the scope of this work. First, ¹D effluent flows from the ¹D column outlet into the capillary for a time that determines the volume of each collected fraction. Then - usually upon a valve switch - the capillary is connected to the ²D pump so that its contents are displaced from the capillary and effectively "injected" into the ²D column. The displacement step can be executed two different ways.

^{*} Corresponding author.

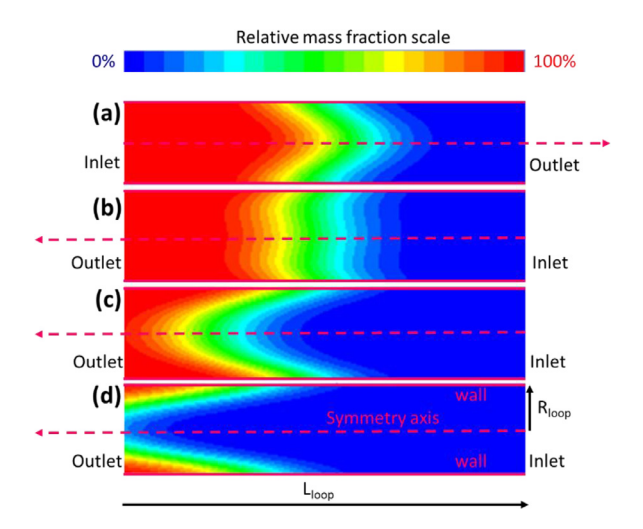


Fig. 1. Illustration of concentration profiles during filling and emptying of a sample loop ($V_{fill} = F_{fill} \cdot t$ and $V_{empty} = F_{empty} \cdot t$). $F_{fill} = 0.25$ mL/min, $F_{empty} = 2$ mL/min, $D_{mol} = 1 \cdot 10^{-9}$ m²/s, $V_{loop} = 160$ μ L, $L_{loop} = 187.1$ cm, $R_{loop} = 175$ μ L. (a) Filling time = 19.2 s, $V_{fill} = 80$ μ L. (b) Emptying time = 0.3 s, $V_{empty} = 10$ μ L. (c) Emptying time = 0.9 s, $V_{empty} = 30$ μ L. (d) Emptying time = 1.8 s, $V_{empty} = 60$ μ L. Aspect ratio was adjusted for clarity by scaling L_{loop} with a factor of 1/1000.

When the fraction is displaced from the capillary in the same flow direction in which it was collected, this is referred to as the "First-In-First-Out" (FIFO) approach. When the fraction is displaced from the capillary in the direction opposite from which it was collected, this is referred to as the "First-In-Last-Out" (FILO) approach. In the literature, different researchers tend to favor either FIFO or FILO, but we are not aware of any thorough, systematic studies of the impact of these modulation approaches (i.e., FIFO and FILO) on the performance of ²D separations. While it seems likely that the impact of the modulation mode will be application dependent, we have shown in our own work that the impact can be significant in at least some cases (e.g., see Fig. S4 in ref [7]). Please note that other notation are used in literature, such as concurrent for FIFO and countercurrent for FILO approaches [7].

The main aim of the present paper is to study dispersion that occurs in an open tubular loop during modulation using the FILO mode. The FIFO case is sufficiently different that we will address it in a different contribution. First, a generalized model will be developed using numerical simulations, which is then verified under realistic experimental conditions. In addition, the effect of coiling the fraction collection loop on peak variances is determined. A similar simulation and experimental study was performed by Samuelsson et al., but this work did not provide a comprehensive framework and model to predict dispersion in a wide range of conditions [8].

2. Experimental

2.1. Numerical simulations

2.1.1. Simulation geometry and boundary conditions

Fig. 1 illustrates the simulation geometry (aspect-ratio scaled with 1/1000) used in this work. The species distribution computed in the actual simulation geometry (i.e., the upper half of each plot) has been mirrored along the symmetry axis to provide a view of the full cross section of the sample loop. By assuming we are working with a straight loop capillary, a 2D axisymmetrical simulation geometry can be used to model the 3D cylindrical loop. This results in a simplified geometry and requires less simulation time. For most conditions, the simulation geometry was a 2D rectangle with a width (R_{loop}) of 175 μ m and a length (L_{loop}) of 187.1 cm resulting in a loop volume of 160 μ L. Only for the conditions where

peak volumes larger than 80 μ L were explored, a larger geometry (360 μ L) was used to avoid sample loss at the outlet [9]. Other widths were simulated only to check if the dimensionless representation used in section 3.1 is valid.

The top edge of the geometry was assigned as a wall with a no-slip boundary condition and a zero normal concentration gradient (i.e., a zero flux wall condition). The bottom edge was assigned as a symmetry axis with a zero normal concentration and velocity gradient. During the filling of the loop, the left side of the geometry (width R_{loop}) is treated as a mass flow inlet while the right side is treated as a pressure outlet with a zero-gauge pressure. To simulate how the loop is emptied (i.e., when the flow is reversed for FILO operation), the boundary conditions for the left and right sides are simply reversed. The different t_{empty}^* (for the definition of t_{empty}^* see section 3.1) and F_{empty}/F_{fill} values considered in this study were the result of different filling flow rates (F_{fill}), loop emptying flow rates (F_{empty}), diffusion coefficients (D_{mol}), and filling volumes (i.e., $V_{fill} = F_{fill} \cdot t_{fill}$).

2.1.2. Simulation procedure and post processing

To simulate the filling process, a step function in mass fraction $(C_{in}=0.01)$ is set at the inlet of the capillary to fill the loop at a flow rate F_{fill} . The duration of the filling step was always chosen such that the total volume of sample entering the loop maximally occupied half the loop volume or less to avoid any analyte loss at the outlet [9]. In the emptying step (Fig. 1b-d), the flow direction is reversed (with a given F_{empty}/F_{fill} ratio), emptying the loaded sample plug out of the same end of the loop from which it was loaded. It is clear from Figs. 1c-d that sample molecules that diffused towards the low velocity region near the wall take a long time to empty from the sample loop. Temporal emptying concentration profiles $C_{out}(t)$ were obtained at the outlet during emptying (i.e., the inlet during sample filling becomes the outlet during emptying) by recording at each time step the flow rate averaged concentrations defined as:

$$C_{out}(t) = \frac{\int_{S} u_{s} \cdot c_{s} \cdot dS}{\int_{S} u_{s} \cdot dS}$$
 (1)

with u_s the local axial velocity across the outlet, c_s the local analyte concentration across the outlet, and S the surface area of the outlet. Normalized emptying profiles were subsequently created by plotting $C_{out}(t)/C_{in}$ as a function of the time t (e.g., see Fig. S1 of the Supplementary Material) or the normalized volumetric equivalent of the time $(F_{empty} \cdot t/V_{fill}, \text{ see Fig. 3a})$.

From the emptying profile, the volumetric peak variance σ_v^2 was calculated using the moment expressions given in Eqs. (2), (3) and (4):

$$MOM_i = \int_0^{t_f} C_{out}(t) \cdot t^i \cdot dt$$
 (2)

$$\sigma_t^2 = \frac{MOM_2}{MOM_0} - \left(\frac{MOM_1}{MOM_0}\right)^2 \tag{3}$$

$$\sigma_V^2 = \sigma_t^2 \cdot F_{empty}^2 \tag{4}$$

With $\mathrm{MOM_i}$ the ith order moment of the concentration profile of the analyte exiting the loop, σ_t^2 the time-based peak variance, F_{empty} the flow rate during displacement of the sample from the loop and t_f the time at which $C_{out}(t)/C_{in}$ drops to 0.001. The latter condition was chosen because this is also the cut-off used to integrate the experimental emptying profiles.

An important assumption made is that the mobile phase entering the loop during filling and emptying of the loop is the same and equal to the composition of the liquid present in the loop before the start of filling (save the addition of the tracer analyte during filling). Given the large number of possible combinations of

mobile phase solvents, we have elected to focus on this case. In practice, differences between the compositions of the solvent entering the loop and solvent remaining in the loop from prior work may lead to effects other than those observed in the present study, including, for example, dynamics effects as a result of differences in viscosities (e.g. viscous fingering), incomplete mixing between the solvents, etc. The interested reader in referred to more specific literature on these topics [10-12].

2.1.3. Mesh

A total of 1,496,700 cells of a rectangular structured grid were used to mesh the modeled 2D geometry. The number of cells along the flow axis was 74,835, whereas 20 cells were used along the radial axis. All cells had an axial length of 25 μ m, while their radial length varied between 1 μ m near the wall and 30 μ m near the symmetry axis with a 1.195 height growth rate, to better capture the larger velocity differences between adjacent cells near the wall.

To perform a grid check, a mesh having four times more cells than the standard grid described above was generated by halving the length and width of each cell. Subsequently, the values of σ_V^2/V_{fill}^2 were calculated using the new grid for a low and a high value of t_{empty}^* (resp., $1\cdot 10^{-5}$ and 0.8) in combination with the two extreme ratios of F_{empty}/F_{fill} (0.7 and 20). The obtained values of σ_V^2/V_{fill}^2 were then compared to their corresponding values obtained by the standard grid. The difference between values obtained using the two grids never exceeded 0.5%. The validity of the standard time step $(1\cdot 10^{-4}~{\rm s})$ was also checked by doing the same comparison as for the grid check. It was found that the difference between the σ_V^2/V_{fill}^2 values obtained with the standard time step and the ones obtained with a time step of $1\times 10^{-5}~{\rm s}$ never exceeded 0.3%.

2.1.4. Solver settings

The velocity and concentration fields were determined by solving the conservation equations for mass and momentum and the convection-diffusion equation using the finite volumes solvers of Ansys Fluent® with double precision. When solving the steady-state velocity fields, the pressure-based coupled solver with second order upwind spatial momentum discretization and second order spatial pressure discretization was used. When solving the transient concentration fields, first order upwind spatial discretization and second order implicit temporal discretization was used. Gradients were evaluated using the Least Squares Cell Based method. More detail regarding the numerical models and simulations can be found in previous works [9,13].

2.1.5. Software and hardware

All simulations were performed with Ansys Fluent 19.2 software on Dell Power Edge R210 Rack Servers, with an Intel Xeon x3460 processor (clock speed 2,8 GHz, 4 cores) and 16 Gb, 1333 MHz ram memory running Windows server edition 2008 R2(64-bit) as an operating system.

2.2. Experimental emptying profiles

All reagents were used as obtained from their respective manufacturers. Methanol (MeOH, HPLC Grade $\geq 99.9\%$), isopropanol (IPA, HPLC Grade $\geq 99.9\%$), and uracil were all obtained from Sigma-Aldrich (St. Louis, MO). Water was purified in-house using a Milli-Q water purification system (Billerica, MA).

The experimental setup used to determine the emptying profiles for the sample loop is illustrated schematically in Fig. 2. Pumps 1 and 2 (G7120A) were binary pumps from Agilent Technologies (Waldbronn, Germany). The 8-port/2-position switching valve (p/n: 5067-4214) and variable wavelength (VWD) UV absorbance detector (G7114B; 2 μ L flow cell G1314-60187) were also

from Agilent. The instrument was controlled using Agilent Chem-Station software (C.01.07 SR3 [465]), and raw absorbance data were exported from ChemStation to .csv files for further treatment.

Emptying profiles were measured using the same 84.1 + - 0.7μL test capillary as described in section 2.3 of the previous paper [9]. Emptying profiles were obtained twice for each condition studied, once with the capillary stretched out straight, and once with the capillary coiled to a diameter of 5.7 cm. The procedure was as follows. First, the loop capillary was flushed with at least three volumes (i.e., about 240 µL) of mobile phase (e.g., 50/50 ACN/H₂O) using Pump 2 as shown in Fig. 2. Then, the valve was switched such that Pump 1 - which pumped the same mobile phase as in Pump 2 but with 10 $\mu g/mL$ of uracil added – was connected to the loop capillary, and filled for an amount of time corresponding to the desired fill volume of 30 µL. Finally, the valve was again switched (the time of the programmed switch was treated as time zero) such that Pump 2 was reconnected to the loop capillary, and data were collected for a time corresponding to three loop volumes of liquid pumped through the capillary. This process was repeated five times, each time resulting in profiles like those shown in Fig. 6b, Fig. S6 (B), and Fig. S7 (B). A list of all experimental settings is given in the Supplementary Material in Tables S1, S2 and

3. Results and discussion

3.1. Simulated concentration profiles and broadening model

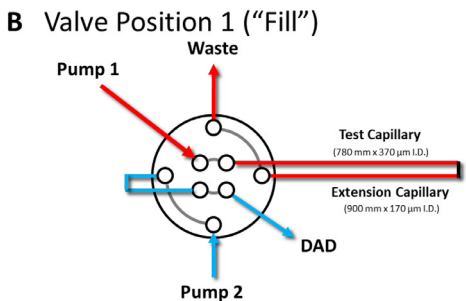
Simulated concentration profiles for the outlet of the loop expressed in volumetric units ($V_{empty} = F_{empty} \cdot t$), and normalized by the volume loaded into the sample loop (V_{fill}), are presented in Fig. 3a for a filling flow rate (F_{fill}) of 0.25 mL/min, an emptying flow rate (F_{empty}) of 2 mL/min ($F_{empty}/F_{fill} = 8$) and four different filling volumes. Non-normalized profiles are shown in Fig. S1 of the Supplementary Material. It is important to note here that the step-like variation in concentration observed at the start of emptying (note: to more clearly represent this, the curve starts at -0.5 on the x-axis) is due to the fact that the emptying profile in this numerical study is monitored directly at the outlet of the capillary in the simulation. This is different from a physical experiment (using e.g. a 2D-LC setup or the one used in Fig. 2) where the injected sample must first travel through a valve and additional connecting capillary before reaching the detector.

A rather complex behavior is found for the different $V_{\it fill}$ values, with the curves crossing multiple times. It is noteworthy that the concentration plateau at the start of emptying step increases with increasing fill volume. It is also interesting that the tailing part obtained for the largest filling volume (red curve) is steeper and shorter than for the smaller volumes. Besides the filling volume, the effects of other parameters including diffusion coefficient, loop diameter and filling/emptying flow ratios were investigated. It was found that perfectly overlapping dimensionless emptying profiles are obtained when two conditions are met. First, the ratio of filling and emptying flow rates $F_{\it empty}/F_{\it fill}$ should be the same. Second, the emptying profiles should have the same dimensionless emptying time constant $t_{\it empty}^*$, defined as:

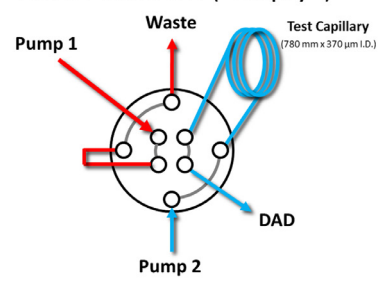
$$t_{empty}^* = \frac{V_{fill} \cdot D_{mol}}{F_{empty} \cdot R_{loop}^2} \tag{5}$$

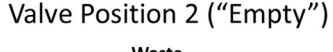
The physical interpretation of this time constant is that it represents the ratio of the time needed to empty the volume equivalent of the fill volume (i.e. V_{fill}/F_{empty}) to the time needed for diffusion across the radius of the loop (i.e., D_{mol}/R_{loop}^2). For example, when considering a sample loop which is twice as wide, the same dimensionless emptying profile is found for a fill volume that is four

A Valve Position 1 ("Fill") Pump 1 Pump 2 B Valve Position 1 ("Fill")



Valve Position 2 ("Empty")





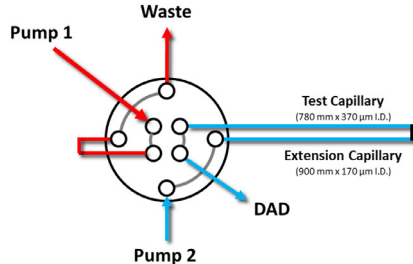


Fig. 2. Schematic representation of experimental setup used to determine the emptying profiles for (A) the capillary coiled and (B) with the capillary stretched out straight. Left panels represent the filling step and right panels the emptying step.

times larger, assuming all other parameters remain the same. This was confirmed by simulating cases with different loop radii, diffusion coefficients, emptying flow rates and diffusion coefficients, but with the same t^*_{empty} in a wide range of t^*_{empty} . The effect of the ratio F_{empty}/F_{fill} on the dimensionless emptying profiles is illustrated in Fig. 3b. It is not surprising that this parameter plays an important role in the shape of the emptying profiles as it, in combination with t_{empty}^* , represents the relative time for radial diffusion during emptying and filling (see also the definition of t_{fill}^* in Eq. (11)). These observations are consistent with the results from Deridder et al. [13] who investigated the band broadening during sample injection using a flow-through needle injection for 1D-LC and noted the emergence of the same two dimensionless numbers. In fact, the geometry and assumptions underlying this earlier study are the same as those presented here. The main physical difference with the flow through-needle injection is that in that case there is usually a few seconds hold between loading sample into the needle and emptying the needle due to the time needed for the needle to move from the sample vial to the needle seat. In 2D-LC, especially in the comprehensive mode of separation (LC \times LC), this time is much shorter, and was assumed to be negligible in the simulations described here. In other 2D-LC applications, such as multiple heartcutting, this assumption is of course no longer valid in the cases where there is a significant (>> 1 s) waiting time between the end of filling, and the start of emptying the loop [13]. Consideration of such cases is beyond the scope of this paper. Since the dimensionless elution profiles are the same when F_{empty}/F_{fill} and t_{empty}^* are constant, the resulting normalized peak widths and peak variances (σ_V/V_{fill}) or σ_V^2/V_{fill}^2) should also be the same if plotted vs. t_{empty}^* for a given ratio of F_{empty}/F_{fill} . This is illustrated in Fig. 3c where we see that varying F_{empty}/F_{fill} produces a curve that goes through a maximum. As previously explained in [13], low values of t_{empty}^* correspond to conditions where the effects of the parabolic flow profile during filling can be entirely compensated during emptying because the analyte molecules entering the tube in the center do not have enough time to diffuse toward the wall before the flow is reversed to empty the tube. At high t_{empty}^{*} the opposite occurs, i.e., there is enough time for radial equilibration during filling and emptying and fewer analyte molecules will trail behind by residing too long in the low velocity regions near the wall. The ratio of F_{empty}/F_{fill} in turn reflects the relative time available for radial equilibration during both steps, affecting the shape of the curve.

Two observations about the effect of F_{empty}/F_{fill} can be made, namely that the maximum value of σ_V^2/V_{fill}^2 increases with increasing F_{empty}/F_{fill} , and that the location of this maximum $(t_{empty}^*)_{max}$ shifts to higher t_{empty}^* values for lower F_{empty}/F_{fill} values. Several other F_{empty}/F_{fill} ratios were investigated to study these variations in more detail. It was found that the value of $(\sigma_V^2/V_{fill}^2)_{max}$ increases linearly with the square root of F_{empty}/F_{fill} in the range of investigated F_{empty}/F_{fill} values (0.7 to 40), as shown in Fig. 4a. The dependence of $(t_{empty}^*)_{max}$ on F_{empty}/F_{fill} was more difficult to model and finally we opted for a power law model with $(F_{fill}/F_{empty})^{0.7}$ (note the inverse ratio used) as shown in Fig. 4b. The resulting fitting functions are given below:

$$\left(\frac{\sigma_V^2}{V_{fill}^2}\right)_{max} = 0.2 + 0.078 \cdot \left(\frac{F_{empty}}{F_{fill}}\right)^{0.5}$$
 (6)

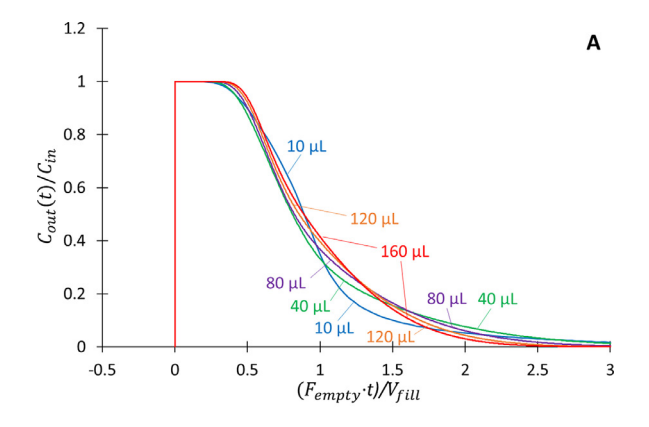
$$(t_{empty}^*)_{max} = 0.06 \cdot \left(\frac{F_{fill}}{F_{empty}}\right)^{0.7}$$
 (7)

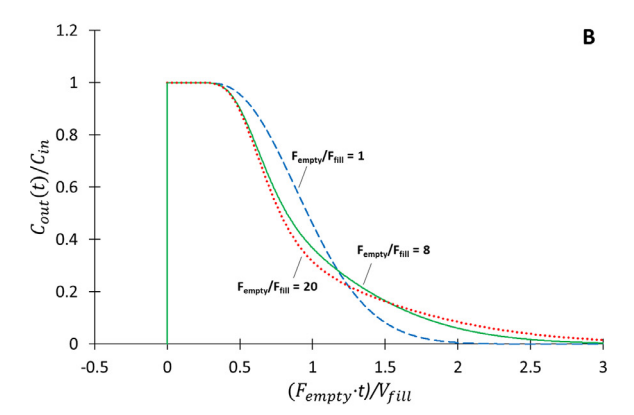
We then investigated if the curves given in Fig. 3c and those for the other investigated F_{empty}/F_{fill} ratios would overlap if the σ_V^2/V_{fill}^2 and t_{empty}^* values would be normalized, i.e., by respectively dividing them by $(\sigma_V^2/V_{fill}^2)_{max}$ and $(t_{empty}^*)_{max}$, yielding the following parameters:

$$Y = \frac{\sigma_V^2}{V_{fill}^2} / \left(\frac{\sigma_V^2}{V_{fill}^2}\right)_{max}$$
 (8)

$$X = ln \left[t_{empty}^* / \left(t_{empty}^* \right)_{max} \right] \tag{9}$$

The results are presented in Fig. 5a, showing a good agreement for the different F_{empty}/F_{fill} curves in the range of values where we have both simulation and experimental results, i.e. -1<X<3 (the entire simulation range is shown in Fig. S2 in supplementary material). The x-axis was converted to the natural logarithm of





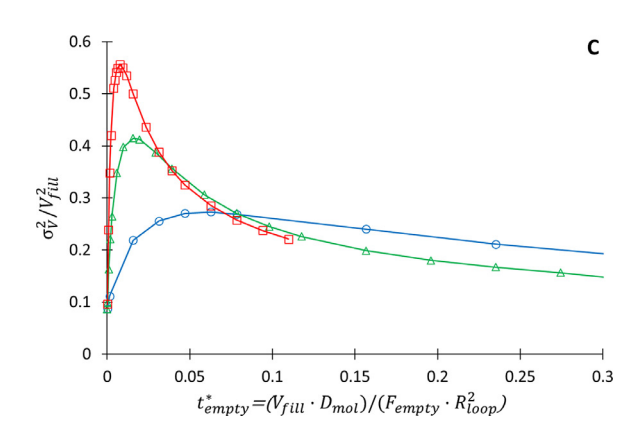
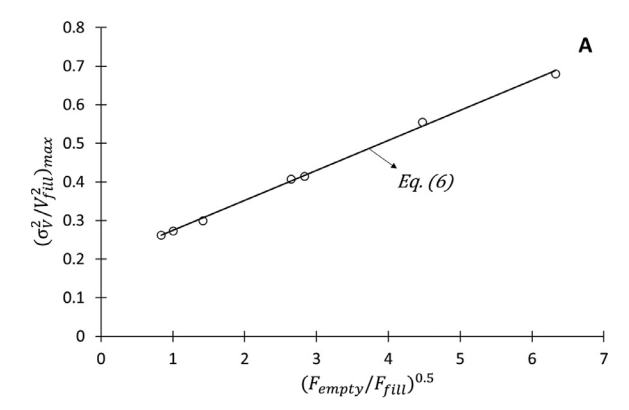


Fig. 3. Simulated normalized emptying profiles as a function of the normalized emptying volume ($F_{empty} \cdot t/V_{fill}$) (A) for different sample volumes ($V_{fill} = 10 \ \mu L$ (blue), 40 μL (green), 80 μL (purple), 120 μL (orange), 160 μL (red)), with $F_{fill} = 0.25$ mL/min, $F_{empty} = 2$ mL/min, $F_{empty}/F_{fill} = 8$ and $D_{mol} = 1 \cdot 10^{-9}$ m²/s. (B) Same data for $V_{fill} = 80$ μL and $F_{fill} = 0.25$ mL/min, but with different $F_{empty}/F_{fill} = 1$ (dashed blue line), $F_{empty}/F_{fill} = 8$ (solid green line), $F_{empty}/F_{fill} = 20$ (dotted red line). (C) Simulated normalized peak variance as a function of dimensionless emptying time for different F_{empty}/F_{fill} ratios: $F_{empty}/F_{fill} = 1$ (blue circles), $F_{empty}/F_{fill} = 8$ (green triangles) and $F_{empty}/F_{fill} = 20$ (red squares). (For interpretation of the references to colour in this figure legend, the reader is referred to the web version of this article.)

 $t^*_{empty}/(t^*_{empty})_{\rm max}$ to better present the range of low t^*_{empty} and because it results in a Gaussian-like shape for the data series, which is also centered around zero (since $\ln(1)=0$). Fitting all the curves for the different F_{empty}/F_{fill} values, the following fit function, which is overlaid in Fig. 5 (full black curve), is found:

$$Y = 0.234 + 0.754 \cdot \exp\left(\frac{-X^2}{4.94}\right) \tag{10}$$

This single equation, in combination with the fit Eqs. (6) and (7), enables prediction of the peak variance for any possible com-



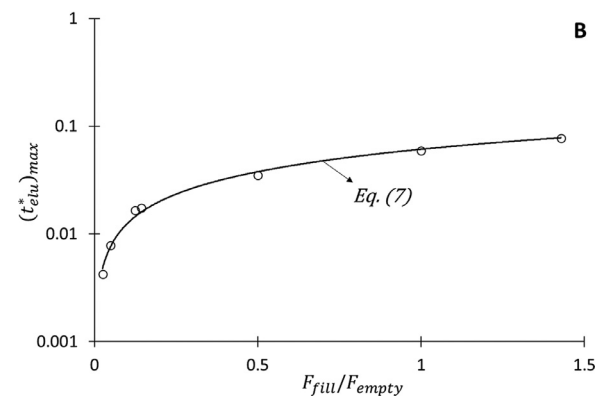


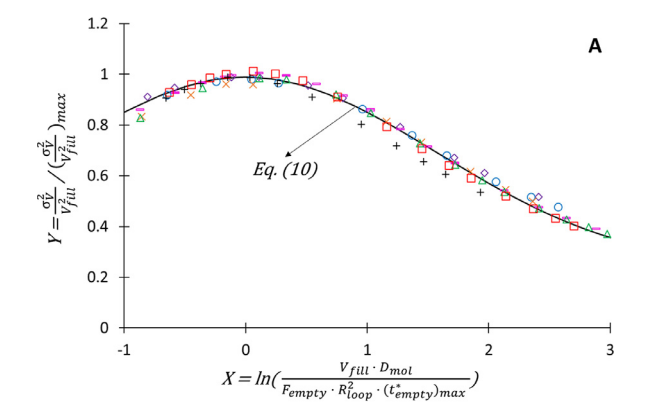
Fig. 4. (A) Plot of the maximum of the simulated normalized peak variance curves as a function of $(F_{empty}|F_{fill})^{0.5}$. (B) Plot of the location of the maximum of the simulated normalized peak variance curves as a function of $F_{fill}|F_{empty}$. The simulated $F_{empty}|F_{fill}|$ ratios are 0.7, 1, 2, 7, 8, 20, 40. The black curves represent the fit equations

bination of D_{mol} , R_{loop} , F_{fill} , F_{empty} , and V_{fill} for all possible F_{empty}/F_{fill} ratios between 0.7 and 40. To further explore the applicability of this fit, the simulations that were carried out with varying V_{fill} were repeated at a fixed value of V_{fill} , but with varying fill and empty flow rates and D_{mol} values, while maintaining a constant F_{empty}/F_{fill} value. These results, which are shown in Fig. 5b, again agree well with the fit function Eq. (10) and confirm that this equation is universally valid as a good estimate for the σ_V^2 value of the concentration profile observed at the loop exit provided that the loop is a straight capillary and operated in the FILO mode. Such predictions can obtained in the following manner:

- 1) values of Y can be calculated for -1 < X < 3 using Eq. (10);
- 2) $(\sigma_V^2/V_{fill}^2)_{max}$ and $(t_{empty}^*)_{max}$ can be determined using Eqs. (6) and (7) for a given value of F_{empty}/F_{fill} , which enables conversion of the X and Y values into a plot of σ_V^2/V_{fill}^2 vs. t_{empty}^* ;
- 3) using the value of t^*_{empty} that can be calculated via Eq. (5) for a given set of conditions $(D_{mol}, R_{loop}, F_{empty}, \text{ and } V_{fill})$ this plot can then be used to find the corresponding σ_v^2 value.

Whereas Fig. 5 compares the fit function with the simulation results in a normalized domain and a logarithmic scale (horizontal axis), Fig. S3 in supplementary materials shows that the agreement between the fit function and the simulated data is equally good in the physical σ_V^2/V_{fill}^2 vs. t_{empty}^* domain, similar to Fig. 3c.

As mentioned above, the ratio F_{empty}/F_{fill} in fact represents the ratio of the times available for analyte molecules to diffuse during the filling and emptying steps. This allows definition of a dimen-



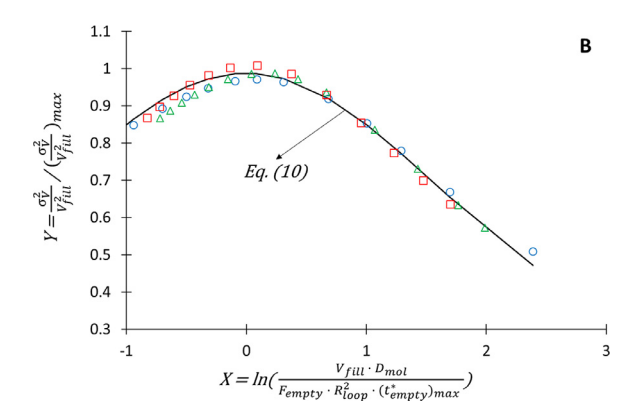


Fig. 5. Fully normalized peak variance fit curve (black solid curve representing the fit Eq. (10)) and the simulated data points obtained (A) using different loop filling volumes for different F_{empty}/F_{fill} ratios: $F_{empty}/F_{fill}=0.7$ (purple diamonds), 1 (blue circles), 2 (orange crosses), 7 (pink hyphens), 8 (green triangles), 20 (red squares), 40 (black pluses). (B) Simulated data obtained using a fixed loop filling volume ($V_{fill}=30~\mu L$). Blue circles: $F_{empty}/F_{fill}=1~$ and $D_{mol}=5.56\cdot 10^{-10}~$ m²/s, green triangles: $F_{empty}/F_{fill}=8~$ and $D_{mol}=5.56\cdot 10^{-10}~$ m²/s, red squares: $F_{empty}/F_{fill}=20~$ and $D_{mol}=2.74\cdot 10^{-10}~$ m²/s. (For interpretation of the references to colour in this figure legend, the reader is referred to the web version of this article.)

sionless fill time t_{fill}^* as:

$$t_{fill}^* = \frac{V_{fill} \cdot D_{mol}}{F_{fill} \cdot R_{loop}^2} \tag{11}$$

Given that the V_{fill} , D_{mol} and R_{loop}^2 values to be used here are the same as those that apply during the emptying step, we can for the case of a straight capillary directly say that $t_{fill}^*/t_{empty}^* = F_{empty}/F_{fill}$. However, the D_{mol} factor is in fact representing the speed of species transport radially in the open tube, which, for purely laminar flow conditions, is only due to diffusion as the radial velocity associated with convective transport is zero, by definition. Since sample loops of the dimensions studied here are usually coiled in practice, at high velocities the resulting centripetal forces can induce secondary radial flows that enhance radial mixing [9,14-21]. For cases where F_{empty} is larger than F_{fill} , which is almost always the case in 2D-LC, it is possible that this enhanced radial dispersion is more pronounced during emptying or even only present during emptying and not during filling. In that case, the factor F_{empty}/F_{fill} should be replaced by t_{fill}^*/t_{empty}^* , where for each t^* the value of D_{mol} should be replaced by the actual radial dispersion coefficient D_{rad} , yielding

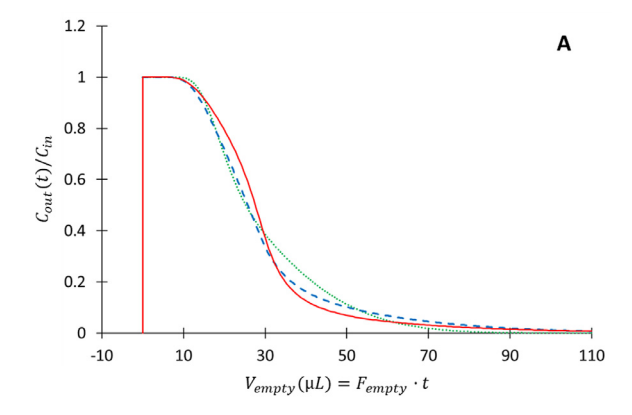
$$\frac{t_{fill}^*}{t_{empty}^*} = \frac{F_{empty} \cdot D_{rad,fill}}{F_{fill} \cdot D_{rad,empty}}$$
(12)

It was therefore of interest to know how this affected the obtained fitting function. Fig. S4 shows a series of data points obtained from simulations where V_{fill} was fixed and F_{empty}/F_{fill} was held constant, but instead of using a fixed D_{mol} value (which will yield the results of Fig. 5b), D_{rad} was applied for the emptying step $(D_{rad,empty})$ and filling $(D_{rad,fill})$. The values of D_{rad} were in fact the value of D_{mol} multiplied by a factor that represents the relative increase in radial transport that depends on the relevant flow rate (i.e., F_{empty} or F_{fill}). To estimate the approximate values of D_{rad} vs. flow rate, data obtained in an earlier study were used (see Fig. 8 in [9]). When comparing the results of these simulations with the fit function when using F_{empty}/F_{fill} , a clear deviation is seen in any case where the flow rate is high enough to result in a $D_{rad} > D_{mol}$. Figure S5 in the supplementary material however shows that if t_{fill}^*/t_{empty}^* is used instead of F_{empty}/F_{fill} with the set $D_{rad,empty}$ and $D_{rad,fill}$ instead of D_{mol} , the fit still accurately predicts σ_V^2/V_{fill}^2 as for the cases with a constant D_{mol} . This again shows the strength of the obtained fitting function as it also enables prediction of the variance of the concentration profile at the loop exit even in cases where radial dispersion plays a role. It is of course required to have reliable data for the dependence of D_{rad} on F. As will be shown in the experimental results section, the dispersion predicted by simulations using D_{mol} in fact represents a limiting worst-case

3.2. Comparison of simulated and experimental emptying

To verify the simulated emptying profiles and the dispersion model given by Eqs. (6)-(10), a series of experimental emptying profiles were measured using a straight loop, as described in Section 2.2. In Fig. 6, simulated emptying profiles (6A) are compared with experimental ones, both obtained at $F_{empty}/F_{fill} = 8$ for different values of t_{empty}^* . The resemblance of the trailing ends of the peaks is striking, even showing very similar behavior in the crossing over of the profiles over the course of the time axis. As previously mentioned, the front of the experimental profile is more rounded than the step-like shape obtained from the simulations due to the dispersion occurring between the outlet of the loop capillary and the UV-detector, which is not included in the simulations. Similarly good agreement between the experimental and simulated profiles was obtained for $F_{empty}/F_{fill} = 1$ and $F_{empty}/F_{fill} = 20$, as shown in Figs. S6 and S7 in the Supplementary Material. To obtain the appropriate range of t_{empty}^* values for the latter case, a more viscous mobile phase was used (isopropanol/water 50/50 v%/v% vs. methanol/water 50/50 v%/v% used for $F_{empty}/F_{fill}=1$ and 8). Under these conditions, the value D_{mol} is reduced by a factor of two [9]. Note that there are small differences in t_{empty}^* due to the difference between simulated and experimentally determined loop radii, and the discretization of the valve switching time (i.e., minimum increment of 0.01 min) that did not allow to exactly obtain the intended $V_{fill} = 30\mu\text{L}$ (see also Tables TS1, TS2 and TS3 in the Supplementary Material).

Using the same method as for the simulated emptying profiles (see Experimental Section Eqs. (1)-((4)), the peak variance of these profiles was determined and, using Eqs. (6)-(9), converted in the same dimensionless representation used in Fig. 5. For the $F_{empty}/F_{fill}=1$, an excellent agreement is found between the fitting function and the experimental results, as shown in Fig. 7. For the two other ratios, an equally good agreement with the fit is found in the range 0 < X < 3. For values of X < 0, a deviation of the experimental results from the fit function is observed, increasing to around 20% at X=-1. The precision of the results in this range is however also poorer as indicated by the increasingly larger error bars $(\pm 1\sigma)$ for lower X values. To obtain these very low X val-



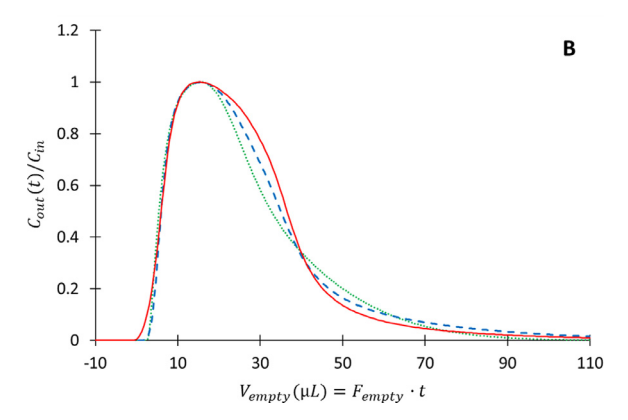


Fig. 6. Normalized emptying profiles as a function of emptying volume for (A) simulated and (B) experimental results. In both cases $F_{empty}/F_{fill}=8$ and $D_{mol}=5.56\cdot 10^{-10}~\text{m}^2/\text{s}$. Green dotted curves: $F_{fill}=0.04~\text{mL/min}$, $F_{empty}=0.32~\text{mL/min}$, $t_{empty,sim}^*=0.102$, $t_{empty,exp}^*=0.091$. Blue dashed curves: $F_{fill}=0.23~\text{mL/min}$, $F_{empty}=1.84~\text{mL/min}$, $t_{empty,sim}^*=0.018$, $t_{empty,exp}^*=0.016$. Red solid curves: $F_{fill}=0.55~\text{mL/min}$, $F_{empty}=4.4~\text{mL/min}$, $t_{empty,sim}^*=0.007$, $t_{empty,exp}^*=0.006$. (For interpretation of the references to colour in this figure legend, the reader is referred to the web version of this article.)

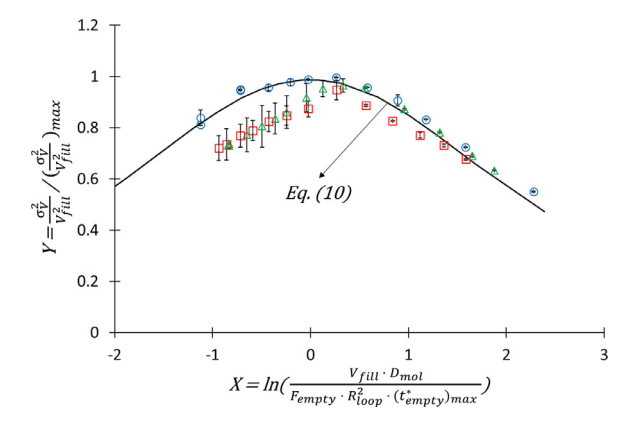


Fig. 7. Fully normalized peak variance fit curve (black solid curve representing the fit Eq. (10)) in addition to the experimental data points obtained using straight loops and with a fixed loop filling volume of V_{fill} =30 μ L. F_{empty}/F_{fill} = 1 and D_{mol} = $5.56 \cdot 10^{-10}$ m²/s (blue circles), F_{empty}/F_{fill} = 8 and D_{mol} = $5.56 \cdot 10^{-10}$ m²/s (green triangles), F_{empty}/F_{fill} = 20 and D_{mol} = $2.74 \cdot 10^{-10}$ m²/s (red squares). (For interpretation of the references to colour in this figure legend, the reader is referred to the web version of this article.)

ues, very high emptying flow rates are used, making these experiments more sensitive to multiple experimental factors including integration errors (narrow peaks) and small variations in the valve switching time (on the order of milliseconds). Nevertheless, the results show that, within acceptable accuracy, the variance of the concentration profile observed at the exit of straight sample loops

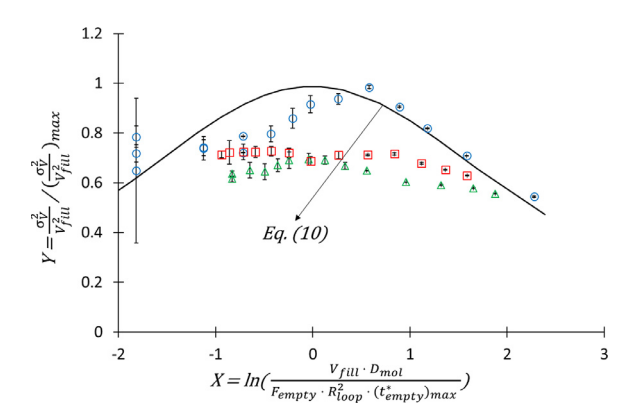


Fig. 8. Fully normalized peak variance fit curve (black solid curve representing the fit Eq. (10)) in addition to the experimental data points obtained using coiled loops and with a fixed loop filling volume of $V_{fill}=30~\mu$ L. $F_{empty}/F_{fill}=1~$ and $D_{mol}=5.56\cdot 10^{-10}~$ m²/s (blue circles), $F_{empty}/F_{fill}=8~$ and $D_{mol}=5.56\cdot 10^{-10}~$ m²/s (green triangles), $F_{empty}/F_{fill}=20~$ and $D_{mol}=2.74\cdot 10^{-10}~$ m²/s (red squares). (For interpretation of the references to colour in this figure legend, the reader is referred to the web version of this article.)

used in the FILO mode, for a wide range of F_{empty}/F_{fill} and t^*_{empty} conditions, can be predicted.

As previously mentioned, the sample loops used in 2D-LC are typically coiled in practice, at least with one half of a turn to make connection to the different valve ports on the modulation valve, but often in multiple turns/coils. As a result, secondary flow effects will occur as the result of centripetal forces, increasing the radial mixing of the analyte with the surrounding solvent, making the system behave as if the analyte has a higher diffusion coefficient. These effects become more pronounced at higher flow rate and as a result the datapoints in the low t^*_{empty} range will be more affected. In addition, whereas for high F_{empty}/F_{fill} ratios, i.e., for low F_{fill} flow rates, this effect only occurs during emptying, for low F_{empty}/F_{fill} ratios (~1) these effects occur to the same extent during both filling and emptying. Fig. 8 shows the experimental results in a way similar to Fig. 7, and using the same loop, but now with the loop coiled (coil dimensions given in the Experimental section) for different F_{empty}/F_{fill} ratios. Whereas for high X values (low velocities) the data agree well with the fitting function, especially for $F_{empty}/F_{fill}=1$, the values increasingly deviate from the fit as X decreases (i.e., for high F_{empty} flow rates). If reliable and accurate data would be available describing the enhancement of the radial dispersion as a function of flow rate, one could try to include these in the theoretical model given by Eqs. (6)-(10), using the t^*_{fill}/t^*_{empty} ratio rather the F_{empty}/F_{fill} ratio. Since this affects both the values of t^*_{empty} and t^*_{fill}/t^*_{empty} (the latter in both numerator and denominator), independent measurements of D_{rad} are thus required to enable this correction.

These results however show that the predictive model obtained and validated for dispersion in the FILO mode in the straight loop provides a "worst-case scenario"-value for the band broadening. For coiled loops, the enhanced radial mixing reduces this band broadening but only to a rather limited extent (max. 40% around the maximum for $F_{empty}/F_{fill}=8$ and 20). The fact that the smallest reduction is found for $F_{empty}/F_{fill}=1$ indicates that the advantages of the enhanced radial transport occurring during the emptying step is countered by that fact that during the filling step this enhanced radial transport tends to increase the amount of solutes that are transported towards the low velocity region near the wall. As for the higher F_{empty}/F_{fill} ratio, the flow rate during emptying is always larger than during filling, thus the enhancement of the radial transport is also always larger than during the filling stage.

4. Conclusions

We draw the following principal conclusions from this study.

- 1. The concentration profiles when emptying straight loops that were filled in the FILO mode without sample loss at the outlet (i.e. 50% or less filling fraction) only depend on the dimensionless emptying time $t^*_{empty} = V_{fill} \cdot D_{mol}/(F_{empty} \cdot R^2_{loop})$ and the ratio of the filling and emptying flow rates F_{empty}/F_{fill} . The shape and relative position of the simulated and experimental elution profiles correspond very well over the entire range of investigated experimental conditions ($F_{empty}/F_{fill} = 1$ -20).
- 2. The dependencies of normalized peak variances on t^*_{empty} depend also on F_{empty}/F_{fill} and go through a maximum. By normalizing these curves for the location and amplitude of this maximum, a universal fit function was developed that allows prediction of the variance of the peaks exiting from straight sample loops over a wide range of t^*_{empty} -values that correspond to most conditions encountered in practice.
- 3. The universal fit function can also be applied in cases where centripetal forces cause secondary flow effects in coiled loops, however this requires the use of the t_{fill}^*/t_{empty}^* -ratio rather than the F_{empty}/F_{fill} -ratio.
- 4. Peak variances are significantly smaller when coiled loops are used compared to straight loops. The straight loop case thus represents the worst-case scenario of the band broadening that can be expected during the filling and emptying of the loop. If very accurate data of the enhanced radial mixing due to centripetal forces as a function of flow rate would be available, one could apply these to the model to improve the prediction for coiled loops.

The trends discussed here should be of great use to practitioners of 2D-LC who are interested in making estimates of the variance of the peaks injected into the second dimension column during method development and optimization. The fact that these variances are exclusively determined by t_{empty}^* and F_{empty}/F_{fill} should allow a relatively straightforward comparison of this injection variance with the expected variance due to dispersion in the second dimension column itself. In addition, this knowledge may influence decision making with respect to the use of active modulation approaches (e.g., Active Solvent Modulation) that can be used to mitigate dispersion of second dimension peaks that can result from unfavorable combinations of solvent composition and volume of fractions injected into the second dimension (i.e., mobile phase mismatch).

Declaration of Competing Interest

The authors declare that they have no known competing financial interests or personal relationships that could have appeared to influence the work reported in this paper.

CRediT authorship contribution statement

Ali Moussa: Conceptualization, Methodology, Validation, Formal analysis, Investigation, Visualization, Writing – original draft, Data curation. Thomas Lauer: Validation, Investigation, Methodology. Dwight Stoll: Conceptualization, Writing – original draft, Writing – review & editing, Supervision, Funding acquisition. Gert Desmet: Conceptualization, Writing – review & editing, Supervision. Ken Broeckhoven: Conceptualization, Formal analysis, Writing – original draft, Writing – review & editing, Resources, Supervision, Funding acquisition.

Acknowledgements

A.M. (grant number: G0D0218N) gratefully acknowledges a research grant from the Research Foundation Flanders (FWO Vlaanderen). The work of T.L. and D.S. on this study has been supported by a grant from the U.S. National Science Foundation (CHE-2003734). All of the instrumentation used to obtain the experimental results was provided by Agilent Technologies.

Supplementary materials

Supplementary material associated with this article can be found, in the online version, at doi:10.1016/j.chroma.2021.462578.

References

- B. Pirok, D. Stoll, P. Schoenmakers, Recent developments in two-dimensional liquid chromatography: fundamental improvements for practical applications, Anal. Chem. 91 (2019) 240–263, doi:10.1021/acs.analchem.8b04841.
- [2] L. Montero, M. Herrero, Two-dimensional liquid chromatography approaches in Foodomics – a review, Anal. Chim. Acta 1083 (2019) 1–18, doi:10.1016/j.aca. 2019.07.036
- [3] D. Stoll, K. Zhang, G. Staples, A. Beck, Recent advances in two-dimensional liquid chromatography for the characterization of monoclonal antibodies and other therapeutic proteins, Adv. Chromatogr., CRC Press 56 (2018) 29–63, doi:10.1201/9780429026171.
- [4] F. Cacciola, K. Arena, F. Mandolfino, D. Donnarumma, P. Dugo, L. Mondello, J. Chromatogr. A 1645 (2021) 462129, doi:10.1016/j.chroma.2021.462129.
- [5] D. Stoll, P. Carr, Two-dimensional liquid chromatography: a state of the art tutorial, Anal. Chem. 89 (2017) 519–531, doi:10.1021/acs.analchem.6b03506.
- [6] Stoll D., Introduction to Two-dimensional liquid chromatography, theory and practice, handbook of advanced chromatography /mass spectrometry techniques, Elsevier, London, pp. 227–286.
- [7] Z.D. Dunn, J. Desai, G.M. Leme, D.R. Stoll, D.D. Richardson, Rapid twodimensional Protein-A size exclusion chromatography of monoclonal antibodies for titer and aggregation measurements from harvested cell culture fluid samples, mAbs 12 (2020) 1702263, doi:10.1080/19420862.2019.1702263.
- [8] J. Samuelsson, L. Edström, P. Forssén, T. Fornstedt, Injection profiles in liquid chromatography. I. A fundamental investigation, J. Chromatogr A. 1217 (2010) 4306–4312, doi:10.1016/j.chroma.2010.04.045.
- [9] A. Moussa, T. Lauer, D.R. Stoll, G. Desmet, K. Broeckhoven, Numerical and experimental investigation of analyte breakthrough from sampling loops used for multi-dimensional liquid chromatography, J. Chromatogr. A 1626 (2020) 461283, doi:10.1016/j.chroma.2020.461283.
- [10] A. Shalliker, H.J. Catchpoole, G.R. Dennis, G. Guiochon, Visualising viscous fingering in chromatography columns: high viscosity solute plug, J. Chromatogr. A. 1142 (2007) 48–55, doi:10.1016/j.chroma.2006.09.059.
- [11] G. Rousseaux, M. Martin, A. De Wit, Viscous fingering in packed chromatographic columns: non-linear dynamics, J. Chromatogr. A. 1218 (2011) 8353– 8361, doi:10.1016/j.chroma.2011.09.040.
- [12] T. Fornstedt, P. Forssén, D. Westerlund, System peaks and their impact in liquid chromatography, TRAC-Trend, Anal. Chem. 81 (2016) 42–50, doi:10.1016/j.trac.
- [13] S. Deridder, G. Desmet, K. Broeckhoven, Numerical investigation of band spreading generated by flow-through needle and fixed loop sample injectors, J. Chromatogr. A 1552 (2018) 29–42, doi:10.1016/j.chroma.2018.04.001.
- [14] E. van Andel, H. Kramers, A. de Voogd, The residence time distribution of laminar flow in curved tubes, Chem. Eng. Sci. 19 (1964) 77–79, doi:10.1016/ 0009-2509(64)85010-7.
- [15] J. Koutsky, R. Adler, Minimisation of axial dispersion by use of secondary flow in helical tubes, Can. J. Chem. Eng. 42 (1964) 239–246, doi:10.1002/cjce. 5450420602.
- [16] S. Berger, L. Talbot, L. Yao, Flow in Curved Pipes, Annu. Rev. Fluid Mech. 15 (1983) 461–512, doi:10.1146/annurev.fl.15.010183.002333.
- [17] A. Shankar, A. Lenhoff, Dispersion in laminar flow in short tubes, AIChE J. 35 (1989) 2048–2052. doi:10.1002/aic.690351218.
- [18] J. Atwood, J. Goldstein, Measurements of diffusion coefficients in liquids at atmospheric and elevated pressure by the chromatographic broadening technique, J. Phys. Chem. 88 (1984) 1875–1885, doi:10.1021/j150653a041.
- [19] L. Janssen, Axial dispersion in laminar flow, Chem. Eng. Sci. 31 (1976) 215–218, doi:10.1016/0009-2509(76)85059-2.
- [20] F. Gritti, S. Shiner, J. Fairchild, G. Guiochon, Evaluation of the kinetic performance of new prototype 2.1 mm \times 100 mm narrow-bore columns packed with 1.6 μ m superficially porous particles, J. Chromatogr. A 1334 (2014) 30–43, doi:10.1016/j.chroma.2014.01.065.
- [21] P. Daskopoulos, A. Lenhoff, Dispersion coefficient for laminar flow in curved tubes, AlChE J. 34 (1988) 2052–2058, doi:10.1002/aic.690341214.